Physics Faculty Research & Creative Works

Physics

01 Mar 1981

Angular Differential and Total Cross Sections for the Excitation of Atomic Hydrogen to Its n=2 State by Helium Ions

Judith E. Aldag

Jerry Peacher
Missouri University of Science and Technology, peacher@mst.edu

Paul J. Martin

V. C. Sutcliffe

et. al. For a complete list of authors, see *https://scholarsmine.mst.edu/phys_facwork/1350*

Recommended Citation

Angular differential and total cross sections for the excitation of atomic hydrogen to its $n = 2$ state by helium ions

J. E. Aldag,* J. L. Peacher, P. J. Martin, V. Sutcliffe,† J. George,‡ E. Redd, T. J. Kvale, D. M. Blankenship, and J. T. Park

*Physics Department, University of Missouri at Rolla, Rolla, Missouri 65401*

Differential cross sections for 15–100 keV He$^+$ excitation of atomic hydrogen to its $n = 2$ level have been determined for c.m. angles from 0 to 8 mrad. The differential cross sections are obtained from an analysis of the angular distribution of the scattered ions which have lost an energy corresponding to the excitation of the target to its $n = 2$ level. The shape of the differential cross section changes rapidly with increasing incident energy. At 15 keV, the differential cross section falls off by a factor of 5 in 6 mrad. At 100 keV, the differential cross section decreases by nearly six orders of magnitude in the same angular range. The higher-energy results are in fair agreement with a recent symmetrized first-order Glauber approximation calculation of the process. Total cross section results are given for the same process in the 15–200 keV range.

I. INTRODUCTION

The results of recent experimental measurements at the University of Missouri-Rolla and theoretical predictions have shown remarkable agreement for angular differential cross sections in the 15–100-keV energy range for proton-atom collisions for relatively simple atomic targets.[1-3] Besides the practical applications of these types of measurements, the results have demonstrated the integrity of the experimental method and contributed to the understanding of the theoretical description of such collisions.

A logical extension of these efforts is presented here. The collision studied involves the excitation of atomic hydrogen during the scattering of a helium ion through the angle θ,

$$\text{He}^+ + \text{H}(1s) \rightarrow \text{He}^+(\theta) + \text{He}^*(n = 2).$$
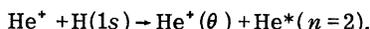
The helium ion-atomic hydrogen collision is the simplest ion-atom collision involving internal structure for both the target and the projectile. Predictions of cross sections involving He$^+$ and H depend only on the scattering theory and approximations because the wave functions for both the He$^+$ and H are known exactly. Thus, comparison of experimental measurements with theory allows a decisive test of the theory.

The measurements were made on the angular energy-loss spectrometer at the University of Missouri at Rolla (UMR). Angular differential cross sections in the energy range of 15–100 keV are presented. Apparent angular differential cross sections are also given for energies up to 200 keV. Total cross section results in the energy range of 15–200 keV are given. The results are compared to the available theoretical treatments[4-8]. No other experimental differential results are available in this energy range. No other total cross section results are available at energies above 30 keV.

II. EXPERIMENTAL METHOD

The energy-loss spectrometer and the general method employed in ion energy-loss spectrometry have been discussed in detail elsewhere.[9-20] The apparatus is a linear accelerator-decelerator combination. The accelerator section includes the ion source and extraction lens, beam focusing, steering, and profile monitoring elements. In this experiment the discharge voltage in the ion source was restricted to voltages less than 40 V. This prevents the formation of He$^+$(2s) excited metastable ions as well as any other excited states which ensures that the incident beam is He$^+$(1s). Between the accelerator and decelerator sections lie the collision region and a magnetic charge/mass analyzer. The decelerator section contains the energy analysis and beam detection apparatus. In the present angular energy-loss spectrometer, the accelerator section and the scattering region are rotated as a unit about an axis that passes through the center of the collision volume, allowing the measurement of cross sections which are differential in both scattering angle and energy loss.

In the present experiment, atomic hydrogen is produced in a variable-angle transmission furnace[2,3,20]. The furnace is constructed of coaxial tungsten tubes and is joule heated to approximately 2700 K. It is similar to those used for earlier total cross section measurements,[16-19] but is much shorter to ensure that the gas containment apertures are not beam definition apertures. The interaction region in the present furnace is about 1 cm long. An accurate determination of this length is not required because the results are

normalized as discussed below.

The molecular hydrogen entering the oven is thermally dissociated. The dissociation fraction was determined using the technique discussed in Refs. 16–19. For each of the three ovens used in this experiment the fraction was greater than 90%. The dissociation fraction does not enter into the cross section determination because the excited states of the H_2 molecule all require higher excitation energy than the $n = 2$ state of atomic hydrogen and would be clearly resolved in the energy loss spectra.

In a collision of an ion and target atom, the scattered ion loses energy to excitation of the target (and/or projectile) and to recoil of the target. The energy full width at half maximum of the peaks in the energy loss spectra were about 1.2 eV in this experiment. The contribution of the energy loss, $e\Delta V$, from target recoil at the largest measurement angle at 100 keV is 0.54 eV larger than the internal energy loss of 10.2 eV. This recoil-corrected energy loss is calculated and set during data acquisition by the controlling minicomputer. The measurement scattering angle, count time, and various emergency and reset signals are also set and monitored. The transmitted ion current and scattering chamber pressure for each measurement are channeled directly to the minicomputer, which corrects the measurement for scattering chamber pressure deviations, instrument and residual-gas caused background, and normal incident beam drift. A standard deviation is calculated for each data point, and the averaged background corrected results are stored for further analysis.

Spectra differential in angle and corresponding to a particular scattering process are measured by selecting the internal energy loss while pivoting the apparatus about the scattering center. The angular distributions of the incident and elastically scattered beam, the energy-loss scattered beam, and corresponding background current distributions measured in this manner comprise a sequence of angular data. Each sequence contains enough information to calculate relative apparent angular differential cross sections directly.

The normalization of these relative results is established by a determination of the density of atomic hydrogen in the scattering region. The total cross section $\sigma(H^+, n = 2)$ for the process $H^+ + H \to H^+ + H(n = 2)$ was established by earlier measurements[16,17] and is used to indicate the target density by probing of the target region with a proton beam. By comparing the total current scattered by this process, $I(H^+, n = 2)$, to the total elastically scattered proton current, $[I_0(H^+)]_f$, the

product of atomic hydrogen target density, n, and scattering region length, l, can be determined from

$$nl = I(H^+, n = 2)/\{\sigma(H^+, n = 2)[I_0(H^+)]_f\}. \quad (1)$$

Because the total cross section, $\sigma(H^+, n = 2)$ was normalized to a Born approximation calculation at 200-keV impact energy,[16,17] the accuracy of the value obtained for nl using Eq. (1) is also dependent on the validity of the Born approximation calculation for 200 keV proton impace excitation of atomic hydrogen. Once the atomic hydrogen density is established, absolute angular differential cross sections can be extracted from the data by established methods[1] and can be integrated to yield total absolute cross sections.

The apparent differential cross section is given as in earlier work[1–3,12–15] by

$$\frac{ds}{d\Omega}(\theta) = \frac{I(\theta)}{nl(I_0)_f \Delta\Omega}. \quad (2)$$

In this expression, $I(\theta)$ is the measured ion current at the angle, θ, corresponding to the inelastic process of interest. The $(I_0)_f$ is the total elastically scattered ion current. The use of $(I_0)_f$ corrects the results for incident beam lost due to charge-changing collisions.[15] The solid angle subtended by the detection window as seen from the scattering center is $\Delta\Omega$. The $ds/d\Omega$ is termed an apparent differential cross section because it is the result of the apparatus averaging the differential cross section over the detection window and the angular distribution of the incident beam.

The data analysis method employed[1] relates this apparent result to the true angular differential cross section for the process, $d\sigma/d\Omega$. The analytical representation of $ds/d\Omega$ involves an integration of the true angular differential cross section over the angular distribution of the incident beam and the solid angle subtended by the detection window. A numerical method has been developed to extract $d\sigma/d\Omega$ by equating the measured $ds/d\Omega$ to its integral representation at each acquisition angle with an assumed form for $d\sigma/d\Omega$.[1]

The data analysis method described in Ref. 1 becomes inadequate when the angular width of the cross section is equal to the angular width of the incident beam distribution. This was encountered in the high-energy data of the present experiment. Therefore, the data for energies between 50 and 100 keV are also analyzed using a "forward modeling" approach. This technique is routinely used in the field of seismic exploration to test the cause of features observed in seismic data.[21] Using the results from the first data-analysis method as a starting point, adjustments are made

to a trial $d\sigma/d\Omega$ using the procedure described in Ref. 21. The trial $d\sigma/d\Omega$ is integrated with the averaged incident beam distribution, $dJ/d\Omega$. The calculated $ds/d\Omega$ obtained in this manner is compared with the measured apparent differential cross section $ds/d\Omega$, to indicate further adjustments to the trial $d\sigma/d\Omega$. This process is continued until the measured and calculated $ds/d\Omega$ differ by typically no more than ten percent at any measurement angle.

In both methods of analysis, the measured and calculated $ds/d\Omega$ are compared point by point to indicate a confidence in the $d\sigma/d\Omega$. This comparison is the most important test of the estimated $d\sigma/d\Omega$. It must be noted that the $d\sigma/d\Omega$ extracted by either data analysis method is not unique. Equally good overall agreement between the measured and calculated $ds/d\Omega$ can be achieved with other slightly different estimations of the form for $d\sigma/d\Omega$, especially for the high-energy results. However, the gross structure of the $d\sigma/d\Omega$ is consistent with the observed $ds/d\Omega$ for all the data presented here.

III. RESULTS

Table I gives the angular differential cross sections for the process $He^+ + H \rightarrow He^+ (\theta) + H^* (n=2)$ at various projectile laboratory incident energies. These results represent some 300 measurements of the angular distributions and an equal number of associated incident, elastically scattered, and background distribution measurements. Data was acquired on three different occasions with somewhat different target furnace conditions in each case. The atomic hydrogen target density was determined in each case as discussed above. The differential cross sections obtained using the different ovens were essentially identical.

In the results tabulated below the incident energy is given in laboratory units. The scattering angle in center of mass units is θ. The averaged extracted differential cross section, $d\sigma/d\Omega$, is

TABLE I. Differential cross sections for excitation of atomic hydrogen to the $n=2$ state by helium-ion impact. (Angles and cross sections are in center-of-mass units. The ion impact energies are given in laboratory units. The $[d\sigma/d\Omega \, (cm^2/sr)]_{fm}$ are the results of the forward modeling procedures discussed in the text.)

Angle (c.m.) (10^{-3} rad)	15 keV (lab) $\frac{d\sigma}{d\Omega}\left(\frac{cm^2}{sr}\right)$	20 keV (lab) $\frac{d\sigma}{d\Omega}\left(\frac{cm^2}{sr}\right)$	25 keV (lab) $\frac{d\sigma}{d\Omega}\left(\frac{cm^2}{sr}\right)$
0.0	$(1.4 \pm 0.4) \times 10^{-12}$	$(4.0 \pm 2.0) \times 10^{-12}$	$(5.8 \pm 2.1) \times 10^{-12}$
0.4	$(1.0 \pm 0.3) \times 10^{-12}$	$(2.3 \pm 1.2) \times 10^{-12}$	$(3.4 \pm 1.3) \times 10^{-12}$
0.8	$(9.7 \pm 2.2) \times 10^{-13}$	$(1.4 \pm 0.4) \times 10^{-12}$	$(1.9 \pm 0.9) \times 10^{-12}$
1.3	$(8.9 \pm 2.6) \times 10^{-13}$	$(1.1 \pm 0.3) \times 10^{-12}$	$(1.4 \pm 0.7) \times 10^{-12}$
1.7	$(7.5 \pm 2.1) \times 10^{-13}$	$(9.0 \pm 2.9) \times 10^{-13}$	$(1.2 \pm 0.7) \times 10^{-12}$
2.1	$(6.9 \pm 2.3) \times 10^{-13}$	$(9.3 \pm 2.9) \times 10^{-13}$	$(1.1 \pm 0.7) \times 10^{-12}$
2.5	$(6.7 \pm 2.1) \times 10^{-13}$	$(8.1 \pm 2.8) \times 10^{-13}$	$(9.4 \pm 5.4) \times 10^{-13}$
3.3	$(5.4 \pm 2.5) \times 10^{-13}$	$(5.6 \pm 1.7) \times 10^{-13}$	$(6.2 \pm 3.8) \times 10^{-13}$
4.2	$(3.9 \pm 1.6) \times 10^{-13}$	$(4.1 \pm 1.3) \times 10^{-13}$	$(4.0 \pm 2.7) \times 10^{-13}$
5.0	$(3.5 \pm 1.4) \times 10^{-13}$	$(2.9 \pm 1.2) \times 10^{-13}$	$(2.8 \pm 1.9) \times 10^{-13}$
5.8	$(2.6 \pm 1.0) \times 10^{-13}$	$(1.9 \pm 1.0) \times 10^{-13}$	$(1.9 \pm 1.4) \times 10^{-13}$
6.7	$(2.1 \pm 0.8) \times 10^{-13}$	$(1.6 \pm 1.0) \times 10^{-13}$	$(1.0 \pm 0.8) \times 10^{-13}$
7.5	$(1.8 \pm 0.6) \times 10^{-13}$	$(1.1 \pm 0.7) \times 10^{-13}$	$(1.1 \pm 0.7) \times 10^{-13}$

Angle (c.m.) (10^{-3} rad)	30 keV (lab) $\frac{d\sigma}{d\Omega}\left(\frac{cm^2}{sr}\right)$	40 keV (lab) $\frac{d\sigma}{d\Omega}\left(\frac{cm^2}{sr}\right)$	45 keV (lab) $\frac{d\sigma}{d\Omega}\left(\frac{cm^2}{sr}\right)$
0.0	$(1.5 \pm 0.7) \times 10^{-11}$	$(4.5 \pm 2.4) \times 10^{-11}$	$(3.2 \pm 0.5) \times 10^{-11}$
0.4	$(7.2 \pm 2.5) \times 10^{-12}$	$(1.6 \pm 0.6) \times 10^{-11}$	$(1.3 \pm 0.2) \times 10^{-11}$
0.8	$(2.7 \pm 1.1) \times 10^{-12}$	$(4.8 \pm 2.4) \times 10^{-12}$	$(4.5 \pm 1.0) \times 10^{-12}$
1.3	$(1.6 \pm 0.8) \times 10^{-12}$	$(2.1 \pm 0.9) \times 10^{-12}$	$(1.6 \pm 0.5) \times 10^{-12}$
1.7	$(1.3 \pm 0.6) \times 10^{-12}$	$(1.2 \pm 0.6) \times 10^{-12}$	$(8.0 \pm 2.9) \times 10^{-13}$
2.1	$(1.0 \pm 0.6) \times 10^{-12}$	$(8.5 \pm 3.3) \times 10^{-13}$	$(4.5 \pm 1.9) \times 10^{-13}$
2.5	$(8.7 \pm 4.7) \times 10^{-13}$	$(6.3 \pm 2.4) \times 10^{-13}$	$(3.1 \pm 1.3) \times 10^{-13}$
3.3	$(5.3 \pm 2.8) \times 10^{-13}$	$(4.0 \pm 2.1) \times 10^{-13}$	$(1.5 \pm 0.7) \times 10^{-13}$
4.2	$(2.9 \pm 1.7) \times 10^{-13}$	$(2.0 \pm 0.9) \times 10^{-13}$	$(8.9 \pm 7.9) \times 10^{-14}$
5.0	$(1.7 \pm 0.9) \times 10^{-13}$	$(1.1 \pm 0.7) \times 10^{-13}$	$(4.3 \pm 2.9) \times 10^{-14}$
5.8	$(1.4 \pm 0.7) \times 10^{-13}$	$(1.2 \pm 1.0) \times 10^{-13}$	$(1.8 \pm 1.6) \times 10^{-14}$
6.7	$(8.3 \pm 4.3) \times 10^{-14}$		$(1.7 \pm 1.4) \times 10^{-14}$
7.5	$(6.8 \pm 5.8) \times 10^{-14}$		

TABLE I. *(Continued.)*

50 keV (lab)

Angle (c.m.) $(10^{-3}$ rad)	$\frac{d\sigma}{d\Omega}\left(\frac{\text{cm}^2}{\text{sr}}\right)$	$\left[\frac{d\sigma}{d\Omega}\left(\frac{\text{cm}^2}{\text{sr}}\right)\right]_{fm}$
0.0	$(8.0 \pm 3.6) \times 10^{-11}$	1.4×10^{-10}
0.4	$(2.8 \pm 1.3) \times 10^{-11}$	3.1×10^{-11}
0.8	$(6.6 \pm 4.1) \times 10^{-12}$	4.4×10^{-12}
1.3	$(2.0 \pm 1.6) \times 10^{-12}$	1.2×10^{-12}
1.7	$(8.7 \pm 6.2) \times 10^{-13}$	8.0×10^{-13}
2.1	$(5.0 \pm 3.0) \times 10^{-13}$	4.8×10^{-13}
2.5	$(3.3 \pm 2.0) \times 10^{-13}$	3.4×10^{-13}
3.3	$(1.6 \pm 1.0) \times 10^{-13}$	1.9×10^{-13}
4.2	$(8.5 \pm 5.6) \times 10^{-14}$	9.6×10^{-14}
5.0	$(4.5 \pm 2.5) \times 10^{-14}$	4.4×10^{-14}
5.8	$(1.3 \pm 0.6) \times 10^{-14}$	1.3×10^{-14}
6.7	$(4.4 \pm 2.5) \times 10^{-15}$	4.8×10^{-15}
7.5	$(2.6 \pm 1.9) \times 10^{-15}$	2.5×10^{-15}

60 keV (lab)

Angle (c.m.) $(10^{-3}$ rad)	$\frac{d\sigma}{d\Omega}\left(\frac{\text{cm}^2}{\text{sr}}\right)$	$\left[\frac{d\sigma}{d\Omega}\left(\frac{\text{cm}^2}{\text{sr}}\right)\right]_{fm}$
0.0	$(1.0 \pm 0.1) \times 10^{-10}$	1.8×10^{-10}
0.4	$(2.7 \pm 0.4) \times 10^{-11}$	2.3×10^{-11}
0.8	$(4.7 \pm 0.9) \times 10^{-12}$	1.6×10^{-12}
1.3	$(1.4 \pm 0.3) \times 10^{-12}$	9.1×10^{-13}
1.7	$(5.1 \pm 0.7) \times 10^{-13}$	4.6×10^{-13}
2.1	$(2.7 \pm 0.5) \times 10^{-13}$	3.0×10^{-13}
2.5	$(1.8 \pm 0.6) \times 10^{-13}$	1.9×10^{-13}
3.3	$(8.0 \pm 0.4) \times 10^{-14}$	8.4×10^{-14}
4.2	$(3.0 \pm 1.3) \times 10^{-14}$	3.0×10^{-14}
5.0	$(2.9 \pm 0.3) \times 10^{-14}$	2.3×10^{-14}
5.8	$(9.6 \pm 0.8) \times 10^{-15}$	1.4×10^{-14}

75 keV (lab)

Angle (c.m.) $(10^{-3}$ rad)	$\frac{d\sigma}{d\Omega}\left(\frac{\text{cm}^2}{\text{sr}}\right)$	$\left[\frac{d\sigma}{d\Omega}\left(\frac{\text{cm}^2}{\text{sr}}\right)\right]_{fm}$
0.0	$(1.4 \pm 0.4) \times 10^{-10}$	5.6×10^{-10}
0.4	$(3.9 \pm 0.3) \times 10^{-11}$	2.5×10^{-11}
0.8	$(7.6 \pm 2.7) \times 10^{-12}$	1.2×10^{-12}
1.3	$(1.5 \pm 0.5) \times 10^{-12}$	4.6×10^{-13}
1.7	$(3.9 \pm 1.4) \times 10^{-13}$	3.0×10^{-13}
2.1	$(1.6 \pm 0.9) \times 10^{-13}$	1.9×10^{-13}
2.5	$(8.6 \pm 5.4) \times 10^{-14}$	1.2×10^{-13}
3.3	$(4.6 \pm 3.2) \times 10^{-14}$	5.2×10^{-14}
4.2	$(2.5 \pm 2.3) \times 10^{-14}$	2.0×10^{-14}
5.0	$(2.3 \pm 1.4) \times 10^{-14}$	1.1×10^{-14}
5.8	$(1.8 \pm 1.4) \times 10^{-14}$	2.9×10^{-14}

100 keV (lab)

Angle (c.m.) $(10^{-3}$ rad)	$\frac{d\sigma}{d\Omega}\left(\frac{\text{cm}^2}{\text{sr}}\right)$	$\left[\frac{d\sigma}{d\Omega}\left(\frac{\text{cm}^2}{\text{sr}}\right)\right]_{fm}$
0.0	$(1.1 \pm 0.5) \times 10^{-10}$	7.9×10^{-10}
0.4	$(3.7 \pm 0.5) \times 10^{-11}$	2.1×10^{-11}
0.8	$(9.1 \pm 4.2) \times 10^{-12}$	1.2×10^{-12}
1.3	$(2.0 \pm 1.4) \times 10^{-12}$	2.2×10^{-13}
1.7	$(4.3 \pm 3.2) \times 10^{-13}$	6.0×10^{-14}
2.1	$(8.0 \pm 6.7) \times 10^{-14}$	3.7×10^{-14}
2.5	$(2.4 \pm 1.6) \times 10^{-14}$	2.6×10^{-14}
3.3	$(1.1 \pm 0.4) \times 10^{-14}$	1.1×10^{-14}
4.2	$(5.3 \pm 3.8) \times 10^{-15}$	5.5×10^{-15}
5.0	$(2.9 \pm 3.5) \times 10^{-15}$	3.2×10^{-15}
5.8	$(1.8 \pm 1.5) \times 10^{-15}$	9.5×10^{-16}

given in center of mass units of cm^2/sr. The results given at each incident energy represent the average of typically ten sequences of angular data. Each sequence contained three measurements of the angular distribution corresponding to the process $\text{He}^+ + \text{H} \to \text{He}^+(\theta) + \text{H}^*(n=2)$.

The data is given in three separate modes. From 15 to 100 keV, differential cross sections were obtained by the numerical extraction method for each sequence of angular data. The averages of these values for $d\sigma/d\Omega$ and their standard deviations are reported. The standard deviations given thus include the effects of any differences resulting from the application of the numerical extraction method to the various sequences of data. From 50 to 100 keV, the results for the differential cross section obtained by the forward modeling method, $(d\sigma/d\Omega)_{fm}$ are also given. The Appendix provides the average apparent differential cross section, $ds/d\Omega$, between 15 and 200 keV. Also included in the Appendix is the normalized average incident ion beam angular distribution, $dJ/d\Omega$. The Appendix includes adequate information to permit the reader to fold his theoretical differential cross section with the experimental ion beam angular distribution for comparison with the experimentally obtained apparent differential cross sections.

Because the time between measurement of the incident and elastically scattered beam distributions and completion of the sequence of data acquisition may be several hours, normal deterioration of the incident beam during data acquisition is unavoidable. A first-order correction for this beam loss is made during data acquisition and data runs were terminated if the incident beam variation exceeded 50% of the initial beam. Despite this fact, the variation in the magnitude of the incident ion current remains the largest single contributor to the statistical error at the smaller scattering angles. This effect contributes directly to the error in the calculation of the ratio $I(\theta)/(I_0)_f$. There is also some indirect contribution in that the term nl of Eq. (2) is determined by similar angular measurements.

The overall uncertainty in the target density is estimated to be 20% and is not included in the errors given in Table I. The statistical errors do not include any uncertainty in the normalization total cross section, $\sigma(\text{H}^+, n=2)$, or any uncertainty indicated by the data analysis method.

The largest potential source of systematic error in the curve shapes is the data analysis method.[1] The analytical representation of $ds/d\Omega$ requires that the incident beam distribution be cylindrically symmetric about the accelerator axis and focused on the scattering center. This

assumption is based on the mechanical design of the apparatus, the method of beam tuning, and the observed angular distribution of the resulting incident beam. The data acquisition technique involves a measurement of the total incident beam current and of the incident beam distribution at each scattering angle. This provides the angular distribution for each data set and permits the verification of the validity of the assumptions of symmetry. To the extent that the beam is symmetric, the measured $ds/d\Omega$ will result in an accurate relative $d\sigma/d\Omega$. For the low-energy results presented here, the systematic errors due to the data analysis method are minimal. The measured angular distributions were broad, and thus the extracted $d\sigma/d\Omega$ differed by only a few percent from the measured $ds/d\Omega$ at each measurement angle. At higher incident energies, the extracted $d\sigma/d\Omega$ and measured $ds/d\Omega$ may differ by factors of 5 or 10 over the measurement range. However, the extracted $d\sigma/d\Omega$ can be shown to be consistent with the measured $ds/d\Omega$ as discussed above.

The most striking feature of the present data is the dramatic change in curve shape as a function of incident energy. While the differential cross section at 15 keV falls by a factor of 5 in 6 mrad, the 50 keV results fall by four orders of magni-

tude and the 100 keV results by almost six orders of magnitude in the same angular range. Some structure is observed in the cross section measurements for impact energies less than 30 keV. In Fig. 1, this structure can be seen as a change in slope in the cross section curve at about 2.5 mrad. Any such structure becomes much less obvious at higher impact energies.

IV. COMPARISON WITH THEORY

The experimentally determined differential cross sections for 25 and 100 keV are shown in Figs. 1 and 2. Shown with them are the results of a symmetrized first-order Glauber treatment,[5] a four-state eikonal treatment,[8] Born approximation calculation results,[8] and for 25 keV, two-state eikonal calculation results.[8] The results of the first-order Glauber approximation[6] are not shown because they are similar to the symmetrized first-order Glauber approximation[5] which provides a better fit to the data.

At 25 keV, no theoretical treatment of the process is in agreement with the present data. In general, the theoretical curves are more sharply peaked than the experimental results. All but the two-state eikonal calculation curve are appreciably
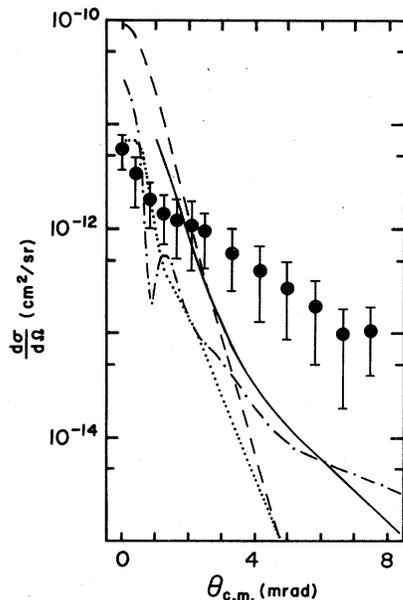
FIG. 1. Angular differential cross section at 25 keV. The solid circles with error bars are the present results. The error bars represent one standard deviation from the mean and include only random statistical error. The curves are the theoretical results: ——— Symmetrized first-order Glauber (Ref. 5); —— —— Born (Ref. 8); ——·—— Four-state eikonal close coupling (Ref. 8); ········ Two-state eikonal close coupling (Ref. 8).
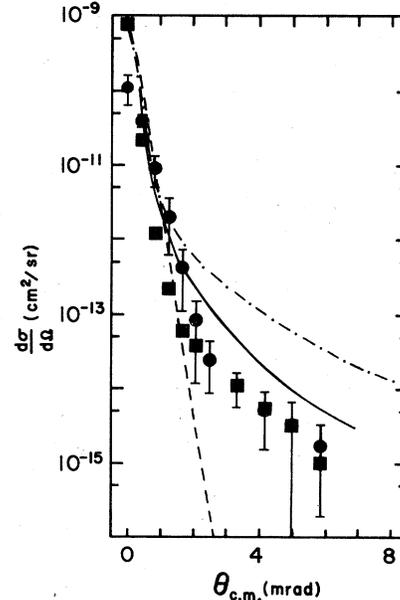
FIG. 2. Angular differential cross section at 100 keV. The solid circles with error bars are the present results. The solid squares are the present results obtained using the forward modeling technique discussed in the text. The error bars represent one standard deviation from the mean and include only random statistical error. The curves are the theoretical results: ——— Symmetrized first-order Glauber (Ref. 5); —— —— Born (Ref. 8); ——·—— Four-state eikonal close coupling (Ref. 8).

larger than the measured result at zero angle. The Born curve is the largest at $\theta = 0$. Both the eikonal curves display structure. The four-state results exhibit a relative minimum at about 0.9 mrad and a relative maximum at about 1.3 mrad. A test using the four-state results in the data analysis program[1] mentioned above indicates that this structure could not be extracted by the data analysis method. The structure observed in the differential cross section curve appears to be at a slightly larger scattering angle than indicated by the four-state theoretical results. In any case the general shape of the four-state theory does not describe the experimental results.

At 50 keV, only the results of the Glauber treatments[5,6] are readily available. Both the first-order Glauber approximation[6] and the symmetrized first-order Glauber approximation[5] results are in good agreement with the experimental curves over much of the range of the data. Both theoretical results lie within the experimental error bars over much of the common angular range.

The present experimental and available theoretical results at 100 keV are shown in Fig. 2. At 100 keV, the two-state eikonal results are significantly different than the four-state values only at $\theta = 0$ and therefore are not shown in Fig. 2. The theoretical calculations are in good agreement with each other and with the experiment at small angles. At larger scattering angles the theory curves diverge significantly. The symmetrized first-order Glauber approximation[5] results are in fair agreement with the experimental results at large angle values, but no theoretical result is in good agreement beyond 2 mrad. The first-order Glauber approximation[6] is higher than the symmetrized first-order Glauber approximation[5] which results in poorer agreement with the experimental data.

V. TOTAL CROSS SECTION RESULTS

The method employed in this experiment was developed to measure differential cross sections. It is not ideal for the measurement of total cross sections. Total cross sections are obtained by integrating $d\sigma/d\Omega$. Because $d\sigma/d\Omega$ decreases so rapidly with angle, the value of its integral is strongly dependent on only one or two measurement points. The result is a large statistical uncertainty in the total measurements shown below. However, these integrations provide the only available measurement of the total cross section for the $He^+ + H \rightarrow He^+ + H^*(n=2)$ cross section for ion impact energies above 30 keV.

Figure 3 displays the total cross section results, σ, determined from the 15–100 keV angular measurements reported here. Also shown for 15–200

keV are apparent total cross section results, s, determined by integration of $ds/d\Omega$, the averaged apparent differential cross section. The error bars shown represent one standard deviation from the mean and include only random statistical error. In the 15–100 keV range, the total and apparent total cross sections are nearly identical. This is to be expected at the lower energies where $d\sigma/d\Omega$ and $ds/d\Omega$ differ only slightly. However, the agreement in the total values extends to 100 keV ion impact energy where $d\sigma/d\Omega$ and $ds/d\Omega$ are very different. Thus, the total cross sections, σ, is expected to follow the integrated apparent value, s, in the 125–200 keV range where reliable results for $d\sigma/d\Omega$ could not be extracted. However, the reliability of the apparent value, s, above 125 keV cannot be documented from the agreement between s and σ at energies below 100 keV.

The magnitude of the incident beam current is smallest at the low-energy end of the operating range of the spectrometer. This places a limit on the angle, θ_{max}, at which a reasonable signal-to-noise ratio can be maintained. As a result, it is estimated by simple extrapolation of the present data that the total cross section for the low-energy results is too low by 5–25% by virtue of this experimental limitation. This estimated correction is not shown in the plotted values or in the error bars of the total cross section results. Also not shown is an estimated 20% uncertainty in the determination of the target density.

Shown in Fig. 3 at energies above 100 keV are total cross section results[19] extracted from
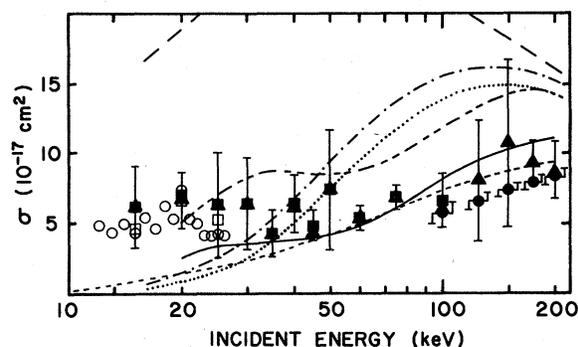
FIG. 3. Total cross section results. The symbols represent experimental results: ■ Present total cross section results (σ); ▲ Present apparent total cross section (s); ● 1976 results (Ref. 19); □ Young et al. (Ref. 22); ○ McKee et al. (Ref. 24). The curves represent theoretical results: — — — First-order Glauber (Ref. 6); ————— Symmetrized first-order Glauber (Ref. 5); — — Born (Refs. 7 and 8); — · — Four-state eikonal close coupling (Refs. 7 and 8); .... Two-state eikonal close coupling (Refs. 7 and 8); — — — — VPSA (Ref. 27).

energy-loss spectra taken with no beam definition or detection apertures present. The cross sections for this type of measurement are obtained as in earlier work.[2,3,16-19] These values are the result of an apparatus integration of the $ds/d\Omega$ in contrast to the numerical integration of $ds/d\Omega$ noted above. The target region used for these measurements was much longer and has been discussed in detail elsewhere.[16-18] These results were normalized as discussed in Sec. IV except that the terms $I(H^+, n=2)$ and $[I_0(H^+)]_f$ of Eq.(1) were determined only from energy-loss spectra for the process $H^+ + H \rightarrow H^+ + H^*(n=2)$. The statistical uncertainties in these results are much smaller than the corresponding values for the total cross section determined by numerical integration of the measured $ds/d\Omega$.

The total measurements obtained by apparatus integration are possibly low due to the scattering of ions outside the acceptance angle of the apparatus. The missing contribution would be from large scattering angles. The present measurements obtained by numerical integration of $ds/d\Omega$, s, would tend to be higher than the actual cross section because at the very highest impact energies the integration is over a slit whose dimensions are not negligible.

The agreement between the results obtained from the two experimental methods is good. The shape of the total cross section curve is probably best represented by the apparatus integrated measurements because these measurements have small statistical uncertainties. The magnitude of the total cross section probably lies between the apparatus integrated results and the results obtained by numerically integrating $ds/d\Omega$. The statistical fluctuations in the total cross section measurements obtained by numerical integration will not support any attempt to find structure in the total cross section curve.

Young *et al.*[22] have reported the cross section for excitation of the $2p$ state of H by 0.5–30 keV He^+-ion impact. Their experiment involved a crossed beam technique and employed an oxygen filter to select the Lyman-α radiation.[23] In a recent experiment, McKee *et al.*[24] measured the cross sections for excitation to the $2s$ and $2p$ states of H by He^+-ion impact. The projectile incident energy was 5–26 keV. Their experimental apparatus and approach was similar to that of Young *et al.*,[22] but included quenching plates to induce emission from the metastable $2s$ state. The results of the Young *et al.*[22] measurement are shown in Fig. 3. The results for the $2s$ excitation process as determined by McKee *et al.*[24] have been added to these measurements to allow comparison with other total cross section results. The

total cross section for the process $He^+ + H \rightarrow He^+ + H^*(n=2)$ as determined by the McKee *et al.*[24] measurements is also shown in Fig. 3. These results are in good agreement with those of Young *et al.*[22] despite a different normalization basis.

Considering the major difference in experimental technique and normalization method, the agreement between the results of these two measurements of the optical emission and the results discussed here is excellent over the common incident energy range. The measurements by angular energy-loss spectrometry are somewhat higher than all of the McKee *et al.*[24] results and most of the Young *et al.*[22] values. However, the values determined in the optical experiments lie well within the error bars of the present measurement.

Also shown in Fig. 3 are the total cross section results obtained for the process $He^+ + H \rightarrow He^+ + H^*(n=2)$ from Born,[7,8] two- and four-state eikonal,[7,8] the first-order Glauber approximation,[6] the symmetrized first-order Glauber approximation,[5] and the Vainshtein-Presnyakov-Sobelman approximation (VPSA).[25] The Born results are higher than all other theoretical and experimental results over the common energy range. Both the two-state and four-state eikonal results are lower than the experimental results below 25 keV and higher above 50 keV. They exhibit more structure than observed experimentally and fall within the experimental error bars only at isolated energies.

The symmetrized first-order Glauber[5] results are in good overall agreement with the experimental values, falling within most of the present error bars, for an energy range from 25–175 keV. The VPSA (Ref. 25) results are also in good agreement with the experimental values over the energy range from 50–200 keV. In contrast to the symmetrized first-order Glauber approximation[5] results and the experimental results, the VPSA (Ref. 25) results monotonically decrease for energies below 50 keV. This is believed[25] to be the result of the inability of the method to account for the temporary formation of $(HeH)^+$ at these energies. The first-order Glauber approximation[6] results differ significantly from the symmetrized first-order Glauber approximation[5] and are in poorer agreement with the experimental results.

VI. DISCUSSION

There are no other experiments reporting angular differential cross sections for the excitation of atomic hydrogen to its $n=2$ level by helium-ion impact in the present energy range. The experimental measurement is a difficult one. The most formidable problem is the detection of

angular changes of the order of the full width at half maximum (FWHM) of the incident angular distribution. In the present case, the FWHM of the measured angular distributions was (1–5) $\times 10^{-4}$ rad in laboratory units. This parameter must be measured in addition to those indicating the initial and final states of the collision partners. The production of atomic hydrogen in a manner which does not complicate the data interpretation is also a troublesome feature of the experiment.

Fayeton et al.[26] have reported angular results for the process of interest in the 750–2500 eV range. Fayeton et al.[26] explained their low-energy results in terms of a $2p\sigma$-$2p\pi$ coupling mechanism. Excitation of the $n=3$ state of the atomic target is not predicted by the $2p\sigma$-$2p\pi$ rotational coupling model. Fayeton et al.[26] have commented on the lack of excitation for $n \geq 3$ states; however, excitation of the $n \geq 3$ states was observed in the present experiment at all energies. The large impact energy difference between the measurement of Fayeton et al.[26] and the present data make it possible that different excitation mechanisms are involved in the two experiments.

The effects of the molecular character of the collision process are also discussed in the paper of Flannery and McCann.[8] Their four-state theory yields a structure in the differential cross section at 25 keV that is not present at 100 keV (incident He$^+$ energy). They have interpreted this structure as a result of the rotational coupling mechanism. Unfortunately, our experimental measurements could not resolve this feature, however, some structure is observed in the 15, 20, 25, and 30 keV cross section curves.

While there is some support for the contributions of rotational coupling excitation mechanisms, the four-state theory which proposes to incorporate this effect does not provide good agreement with the data. The inclusion of charge transfer in a multistate theory might improve the agreement. It appears that a successful theoretical model of the collisional process in the 15 to 30 keV ion impact-energy range will have to incorporate direct excitation, charge transfer, and excitation through the $2p\sigma$-$2p\pi$ rotational coupling mechanism.

Bell and Kingston[27] do not show their total cross section results for helium-ion impact energies less than 400 keV. However, they imply that inclusion of the projectile $n=2$ states in their seven-state close coupling calculation of the total cross section does not produce any significant changes from the four-state calculation of Flannery and McCann.[8] They do note differences for helium-ion impact energies greater than 400 keV. It is pos-

sible that including charge transfer in the close coupling calculations would have a more significant effect in the 15–200 keV energy range.

For the higher energy range (50–200 keV) the results of the Born,[7,8] two- and four-state eikonal[7,8] first-order and symmetrized first-order Glauber,[5,6] and VPSA[25] exhibit varying agreement with the experimental results. No single theory provides excellent agreement with the experimental results for both total and differential cross sections.

The various results at 25 keV (see Figs. 1 and 3) show that the merit of a particular theoretical approximation cannot be determined by comparing only the theoretical results for the total cross section with the experimentally determined values. Both the symmetrized first-order Glauber[5] and four-state eikonal[7,8] total cross section values are in reasonably good agreement with those provided by experiment. However, the theoretical and experimental differential results are clearly different (see Fig. 1).

This experiment provides the only measurement of angular differential cross sections for helium-ion excitation of the $n=2$ state of hydrogen in the 15–100 keV energy range and the only measurement of total cross sections for helium-ion impact energies greater than 30 keV. The experiment covers an energy and angular range in which the available theories diverge significantly. In the energy range covered by the experiment, the angular differential cross sections display a dramatic change in curve shape which is not fully predicted by any of the available theoretical efforts. The agreement between experiment and available theory especially in the 15–30-keV impact-energy is not satisfactory. The agreement at higher energies is better. Of the available theories the symmetrized first-order Glauber results[5] provide the best agreement with the experiment but none of the theoretical efforts adequately describe the differential cross section results. Additional theoretical studies of the He$^+$ + H(1s) → He$^+$(θ) + H*($n=2$) collision are needed. The large dynamic range of the reported measurements will permit a meaningful test of theoretical efforts to model this ion-atom collision process in the 15–200 keV impact-energy range.

ACKNOWLEDGMENT

APPENDIX

The apparent differential cross section is given in Table II. Both the scattering angle and the

J. E. ALDAG *et al.*

TABLE II. Apparent angular differential cross sections. (Angle and cross sections are in center-of-mass coordinates.)

Laboratory incident energy θ(rad)	15 keV $\frac{ds}{d\Omega}$ (cm^2/sr)	20 keV $\frac{ds}{d\Omega}$ (cm^2/sr)	25 keV $\frac{ds}{d\Omega}$ (cm^2/sr)	30 keV $\frac{ds}{d\Omega}$ (cm^2/sr)
0	1.1×10^{-12}	2.4×10^{-12}	2.7×10^{-12}	6.5×10^{-12}
4.16×10^{-4}	9.6×10^{-13}	1.9×10^{-12}	2.3×10^{-12}	5.0×10^{-12}
8.33×10^{-4}	8.8×10^{-13}	1.4×10^{-12}	1.7×10^{-12}	2.7×10^{-12}
1.25×10^{-3}	8.1×10^{-13}	1.1×10^{-12}	1.3×10^{-12}	1.6×10^{-12}
1.67×10^{-3}	6.9×10^{-13}	8.9×10^{-13}	9.9×10^{-13}	1.2×10^{-12}
2.08×10^{-3}	6.1×10^{-13}	8.7×10^{-13}	8.4×10^{-13}	9.0×10^{-13}
2.50×10^{-3}	5.8×10^{-13}	7.7×10^{-13}	7.6×10^{-13}	7.7×10^{-13}
3.33×10^{-3}	4.7×10^{-13}	5.6×10^{-13}	5.4×10^{-13}	4.9×10^{-13}
4.16×10^{-3}	3.5×10^{-13}	4.2×10^{-13}	3.7×10^{-13}	2.9×10^{-13}
5.00×10^{-3}	3.4×10^{-13}	3.0×10^{-13}	2.6×10^{-13}	1.7×10^{-13}
5.83×10^{-3}	2.5×10^{-13}	2.1×10^{-13}	1.9×10^{-13}	1.3×10^{-13}
6.66×10^{-3}	2.1×10^{-13}	1.6×10^{-13}	1.0×10^{-13}	8.8×10^{-14}
7.49×10^{-3}	1.8×10^{-13}	1.1×10^{-13}	9.4×10^{-14}	6.5×10^{-14}

θ(rad)	35 keV $\frac{ds}{d\Omega}$ (cm^2/sr)	40 keV $\frac{ds}{d\Omega}$ (cm^2/sr)	45 keV $\frac{ds}{d\Omega}$ (cm^2/sr)	50 keV $\frac{ds}{d\Omega}$ (cm^2/sr)
0	5.5×10^{-12}	1.6×10^{-11}	8.7×10^{-12}	2.8×10^{-11}
4.16×10^{-4}	4.3×10^{-12}	9.8×10^{-12}	7.1×10^{-12}	2.0×10^{-11}
8.33×10^{-4}	2.5×10^{-12},	4.4×10^{-12}	4.3×10^{-12}	9.7×10^{-12}
1.25×10^{-3}	1.3×10^{-12}	2.2×10^{-12}	2.1×10^{-12}	3.1×10^{-12}
1.67×10^{-3}	7.9×10^{-13}	1.3×10^{-12}	1.1×10^{-12}	1.1×10^{-12}
2.08×10^{-3}	6.1×10^{-13}	9.0×10^{-13}	5.7×10^{-13}	6.0×10^{-13}
2.50×10^{-3}	4.7×10^{-13}	6.3×10^{-13}	3.8×10^{-13}	3.9×10^{-13}
3.33×10^{-3}	2.7×10^{-13}	3.6×10^{-13}	1.8×10^{-13}	1.9×10^{-13}
4.16×10^{-3}	1.6×10^{-13}	2.0×10^{-13}	9.5×10^{-14}	9.6×10^{-14}
5.00×10^{-3}	9.7×10^{-14}	1.2×10^{-13}	4.9×10^{-14}	4.9×10^{-14}
5.83×10^{-3}	6.2×10^{-14}	7.7×10^{-14}	2.0×10^{-14}	1.6×10^{-14}
6.66×10^{-3}	3.6×10^{-14}		1.6×10^{-14}	5.5×10^{-15}
7.49×10^{-3}				2.6×10^{-15}

θ(rad)	60 keV $\frac{ds}{d\Omega}$ (cm^2/sr)	75 keV $\frac{ds}{d\Omega}$ (cm^2/sr)	100 keV $\frac{ds}{d\Omega}$ (cm^2/sr)	125 keV $\frac{ds}{d\Omega}$ (cm^2/sr)
0	2.8×10^{-11}	3.9×10^{-11}	1.8×10^{-11}	7.3×10^{-11}
4.16×10^{-4}	2.0×10^{-11}	2.5×10^{-11}	1.6×10^{-11}	4.1×10^{-11}
8.33×10^{-4}	7.0×10^{-12}	1.0×10^{-11}	9.8×10^{-12}	1.0×10^{-11}
1.25×10^{-3}	2.0×10^{-12}	2.8×10^{-12}	4.5×10^{-12}	1.3×10^{-12}
1.67×10^{-3}	6.8×10^{-13}	7.1×10^{-13}	1.2×10^{-12}	3.2×10^{-13}
2.08×10^{-3}	3.4×10^{-13}	2.7×10^{-13}	2.3×10^{-13}	1.3×10^{-13}
2.50×10^{-3}	2.1×10^{-13}	1.3×10^{-13}	5.8×10^{-14}	5.8×10^{-14}
3.33×10^{-3}	9.4×10^{-14}	5.7×10^{-14}	1.6×10^{-14}	2.6×10^{-14}
4.16×10^{-3}	3.4×10^{-14}	2.7×10^{-14}	6.2×10^{-15}	1.5×10^{-14}
5.00×10^{-3}	2.3×10^{-14}	1.4×10^{-14}	3.6×10^{-15}	
5.83×10^{-3}	1.4×10^{-14}	2.3×10^{-14}	1.3×10^{-15}	

θ(rad)	150 keV $\frac{ds}{d\Omega}$ (cm^2/sr)	175 keV $\frac{ds}{d\Omega}$ (cm^2/sr)	200 keV $\frac{ds}{d\Omega}$ (cm^2/sr)
0	7.9×10^{-11}	4.5×10^{-11}	4.6×10^{-11}
4.16×10^{-4}	4.9×10^{-11}	3.6×10^{-11}	3.5×10^{-11}
8.33×10^{-4}	1.7×10^{-11}	1.7×10^{-11}	1.4×10^{-11}
1.25×10^{-3}	2.6×10^{-12}	3.6×10^{-12}	2.7×10^{-12}
1.67×10^{-3}	4.4×10^{-13}	3.4×10^{-13}	3.8×10^{-13}
2.08×10^{-3}	1.3×10^{-13}	7.2×10^{-14}	4.6×10^{-13}
2.50×10^{-3}	5.0×10^{-14}	4.0×10^{-14}	5.9×10^{-13}
3.33×10^{-3}	1.6×10^{-14}	3.7×10^{-14}	
4.16×10^{-3}	9.5×10^{-15}		

TABLE III. Incident beam distributions. (Angle and beam distributions are in laboratory coordinates.)

θ (rad)	15 keV $\frac{dJ}{d\Omega}$ (sr⁻¹)	20 keV $\frac{dJ}{d\Omega}$ (sr⁻¹)	25 keV $\frac{dJ}{d\Omega}$ (sr⁻¹)
0	1.4×10^7	2.0×10^7	1.4×10^7
6.66×10^{-5}	1.2×10^7	1.5×10^7	1.2×10^7
1.33×10^{-4}	6.6×10^6	6.1×10^6	6.2×10^6
2.00×10^{-4}	2.1×10^6	1.8×10^6	2.5×10^6
2.67×10^{-4}	5.7×10^5	3.4×10^5	6.6×10^5
3.33×10^{-4}	1.9×10^5	4.5×10^4	1.1×10^5
4.00×10^{-4}	8.1×10^4	5.6×10^3	2.0×10^4

θ (rad)	30 keV	35 keV	40 keV
0	2.2×10^7	1.2×10^7	3.5×10^7
6.66×10^{-5}	1.4×10^7	9.7×10^6	1.5×10^7
1.33×10^{-4}	6.3×10^6	5.4×10^6	4.3×10^6
2.00×10^{-4}	1.8×10^6	2.7×10^6	1.8×10^6
2.67×10^{-4}	3.6×10^5	1.0×10^6	6.9×10^5
3.33×10^{-4}	3.7×10^4	3.9×10^5	2.3×10^5
4.00×10^{-4}	6.1×10^3	1.1×10^5	7.1×10^4

θ (rad)	45 keV	50 keV	60 keV
0	1.2×10^7	2.0×10^7	2.3×10^7
6.66×10^{-5}	9.8×10^6	1.5×10^7	1.7×10^7
1.33×10^{-4}	5.3×10^6	6.4×10^6	5.7×10^6
2.00×10^{-4}	2.4×10^6	1.7×10^6	1.7×10^6
2.67×10^{-4}	1.1×10^6	3.3×10^5	2.5×10^5
3.33×10^{-4}	4.9×10^5	4.7×10^4	1.7×10^4
4.00×10^{-4}	2.1×10^5	8.1×10^3	2.2×10^3

θ (rad)	75 keV	100 keV	125 keV
0	1.7×10^7	7.8×10^6	2.1×10^7
6.66×10^{-5}	1.3×10^7	7.0×10^6	1.5×10^7
1.33×10^{-4}	5.9×10^6	5.0×10^6	6.6×10^6
2.00×10^{-4}	2.1×10^6	3.0×10^6	1.6×10^6
2.67×10^{-4}	5.7×10^5	1.5×10^6	2.8×10^5
3.33×10^{-4}	1.4×10^5	5.5×10^5	1.2×10^4
4.00×10^{-4}	3.5×10^4	1.2×10^5	3.0×10^2

θ (rad)	150 keV	175 keV	200 keV
0	1.7×10^7	1.5×10^7	1.3×10^7
6.66×10^{-5}	1.2×10^7	1.3×10^7	1.1×10^7
1.33×10^{-4}	5.6×10^6	7.0×10^6	6.5×10^6
2.00×10^{-4}	2.3×10^6	2.2×10^6	2.7×10^6
2.67×10^{-4}	7.5×10^5	3.5×10^5	5.8×10^5
3.33×10^{-4}	1.7×10^5	1.2×10^4	5.5×10^4
4.00×10^{-4}	1.8×10^4	4.2×10^2	2.2×10^3

apparent differential cross section are expressed in center of mass units in Table II. The averaged normalized incident beam distribution is tabulated in laboratory units in Table III. In Table III, θ is the measurement angle in laboratory units of radians. Tabulation of $ds/d\Omega$ and $dJ/d\Omega$ allows the reader to verify the present data analysis methods, to test other analysis methods, or to compare other determinations of $d\sigma/d\Omega$ to the measured apparent results given here. For a trial $d\sigma/d\Omega$, the corresponding calculated $ds/d\Omega$ is given by

$$\frac{ds}{d\Omega}(\theta) = \frac{1}{\Delta x \Delta y} \int_{-\Delta x/2}^{\Delta x/2} \int_{-\Delta y/2}^{\Delta y/2} \int_0^{2\pi} \int_0^{\alpha_{max}} \frac{dJ}{d\Omega}(\alpha) \frac{d\sigma}{d\Omega}(\Theta)$$
$$\times \sin\alpha \, d\alpha \, d\beta \, dx \, dy \,, \qquad \text{(A1)}$$

where $\Delta x = 9.2 \times 10^{-4}$ cm, $\Delta y = 1.3 \times 10^{-3}$ cm, and $\alpha_{max} = 4 \times 10^{-4}$ rad. The angle, θ, corresponds to the center of the detector window as measured from the accelerator axis.

Also,

$$\cos\Theta = \sin\alpha \, \sin\theta' \cos(\beta - \phi') + \cos\alpha \, \cos\theta' \,, \quad \text{(A2)}$$

with

$$\theta' = \tan^{-1}\left(\frac{(x\cos\theta - z\sin\theta)^2 + y^2}{x\sin\theta + z\cos\theta}\right)^{1/2}, \qquad \text{(A3)}$$

and

$$\phi' = \tan^{-1}\left(\frac{y}{x\cos\theta + z\sin\theta}\right), \qquad \text{(A4)}$$

where $z = 208$ cm. Note that the $dJ(\alpha)/d\Omega$, Δx, Δy, and α_{max} are given in laboratory units. The trial $d\sigma/d\Omega$ and the tabulated $ds/d\Omega$ must be converted to laboratory coordinates for these calculations.

*Present address: Conoco Inc., 1000 South Pine, Ponca City, Oklahoma 74601.
†Present address: Texas Instruments Incorporated, Semiconductor Research Lab, P.O. Box 225012, Mail Stop 82, Dallas, Texas 72565.
‡Present address: 4231 N. 44th Street, Phoenix, Ariz. 85018.
[1]J. T. Park, J. M. George, J. L. Peacher, and J. E. Al-

dag, Phys. Rev. A 18, 48 (1978).
[2]J. T. Park, J. E. Aldag, J. L. Peacher, and J. M. George, Phys. Rev. Lett. 40, 1646 (1978).
[3]J. T. Park, J. E. Aldag, J. L. Peacher, and J. M. George, Phys. Rev. A 21, 751 (1980).
[4]V. Franco, Phys. Lett. 71A, 29 (1979).
[5]V. Franco, Phys. Rev. Lett. 42, 759 (1979).
[6]V. Franco, Phys. Rev. A 20, 2297 (1979).

[7]M. R. Flannery, J. Phys. B **2**, 1044 (1969).

[8]M. R. Flannery and K. J. McCann, J. Phys. B **7**, 1349 (1974).

[9]J. T. Park and F. D. Schowengerdt, Rev. Sci. Instrum. **40**, 753 (1969).

[10]J. T. Park and F. D. Schowengerdt, Phys. Rev. **185**, 152 (1969).

[11]G. W. York, Jr., J. T. Park, J. J. Miskinis, D. H. Crandall, and V. Pol, Rev. Sci. Instrum. **43**, 230 (1972).

[12]V. Pol, W. Kauppila, and J. T. Park, Phys. Rev. A **8**, 2990 (1973).

[13]J. T. Park, V. Pol, J. Lawler, and J. George, Phys. Rev. Lett. **30**, 1013 (1973).

[14]J. T. Park, V. Pol, J. Lawler, J. George, J. Aldag, J. Parker, and J. L. Peacher, Phys. Rev. A **11**, 857 (1975).

[15]J. T. Park, in *Collision Spectroscopy*, edited by R. G. Cooks (Plenum, New York, 1978), pp. 19–90.

[16]J. T. Park, J. E. Aldag, and J. M. George, Phys. Rev. Lett. **34**, 1253 (1975).

[17]J. T. Park, J. E. Aldag, J. M. George, and J. L. Peacher, Phys. Rev. A **14**, 608 (1976).

[18]J. T. Park, J. E. Aldag, J. M. George, J. L. Peacher, and J. H. McGuire, Phys. Rev. A **15**, 508 (1977).

[19]J. E. Aldag, J. M. George, and J. T. Park, Bull. Am. Phys. Soc. **21**, 1264 (1976).

[20]J. M. George, Ph.D. thesis, University of Missouri-Rolla, 1978 (unpublished).

[21]Kenneth H. Waters, *Reflection Seismology* (Wiley, New York, 1978), pp. 315–324.

[22]R. A. Young, R. F. Stebbings, and J. W. McGowan, Phys. Rev. **171**, 85 (1968).

[23]W. L. Fite and R. T. Brackman, Phys. Rev. **112**, 1151 (1958).

[24]J. D. A. McKee, J. R. Sheridan, J. Geddes, and H. B. Gilbody, J. Phys. B **10**, 1679 (1977).

[25]C. E. Theodosiou (private communication).

[26]J. Fayeton, J. C. Houver, M. Barat, and F. Masnou-Seeuws, J. Phys. B **9**, 461 (1976).

[27]K. L. Bell and A. E. Kingston, J. Phys. B **11**, 1259 (1978).